

Measurement of the $e^+e^- \rightarrow \Lambda\bar{\Lambda}$ cross section from threshold to 3.00 GeV using events with initial-state radiation

M. Ablikim,¹ M. N. Achasov,^{13,b} P. Adlarson,⁷³ R. Aliberti,³⁴ A. Amoroso,^{72a,72c} M. R. An,³⁸ Q. An,^{69,56} Y. Bai,⁵⁵ O. Bakina,³⁵ I. Balossino,^{29a} Y. Ban,^{45,g} V. Batozskaya,^{1,43} K. Begzsuren,³¹ N. Berger,³⁴ M. Berlowski,⁴³ M. Bertani,^{28a} D. Bettoni,^{29a} F. Bianchi,^{72a,72c} E. Bianco,^{72a,72c} J. Bloms,⁶⁶ A. Bortone,^{72a,72c} I. Boyko,³⁵ R. A. Briere,⁵ A. Brueggemann,⁶⁶ H. Cai,⁷⁴ X. Cai,^{1,56} A. Calcaterra,^{28a} G. F. Cao,^{1,61} N. Cao,^{1,61} S. A. Cetin,^{60a} J. F. Chang,^{1,56} T. T. Chang,⁷⁵ W. L. Chang,^{1,61} G. R. Che,⁴² G. Chelkov,^{35,a} C. Chen,⁴² Chao Chen,⁵³ G. Chen,¹ H. S. Chen,^{1,61} M. L. Chen,^{1,56,61} S. J. Chen,⁴¹ S. M. Chen,⁵⁹ T. Chen,^{1,61} X. R. Chen,^{30,61} X. T. Chen,^{1,61} Y. B. Chen,^{1,56} Y. Q. Chen,³³ Z. J. Chen,^{25,h} W. S. Cheng,^{72c} S. K. Choi,¹⁰ X. Chu,⁴² G. Cibinetto,^{29a} S. C. Coen,⁴ F. Cossio,^{72c} J. J. Cui,⁴⁸ H. L. Dai,^{1,56} J. P. Dai,⁷⁷ A. Dbeysyi,¹⁹ R. E. de Boer,⁴ D. Dedovich,³⁵ Z. Y. Deng,¹ A. Denig,³⁴ I. Denysenko,³⁵ M. Destefanis,^{72a,72c} F. De Mori,^{72a,72c} B. Ding,^{64,1} X. X. Ding,^{45,g} Y. Ding,³³ Y. Ding,³⁹ J. Dong,^{1,56} L. Y. Dong,^{1,61} M. Y. Dong,^{1,56,61} X. Dong,⁷⁴ S. X. Du,⁷⁹ Z. H. Duan,⁴¹ P. Egorov,^{35,a} Y. L. Fan,⁷⁴ J. Fang,^{1,56} S. S. Fang,^{1,61} W. X. Fang,¹ Y. Fang,¹ R. Farinelli,^{29a} L. Fava,^{72b,72c} F. Feldbauer,⁴ G. Felici,^{28a} C. Q. Feng,^{69,56} J. H. Feng,⁵⁷ K. Fischer,⁶⁷ M. Fritsch,⁴ C. Fritsch,⁶⁶ C. D. Fu,¹ J. L. Fu,⁶¹ Y. W. Fu,¹ H. Gao,⁶¹ Y. N. Gao,^{45,g} Yang Gao,^{69,56} S. Garbolino,^{72c} I. Garzia,^{29a,29b} P. T. Ge,⁷⁴ Z. W. Ge,⁴¹ C. Geng,⁵⁷ E. M. Gersabeck,⁶⁵ A. Gilman,⁶⁷ K. Goetzen,¹⁴ L. Gong,³⁹ W. X. Gong,^{1,56} W. Gradl,³⁴ S. Gramigna,^{29a,29b} M. Greco,^{72a,72c} M. H. Gu,^{1,56} Y. T. Gu,¹⁶ C. Y. Guan,^{1,61} Z. L. Guan,²² A. Q. Guo,^{30,61} L. B. Guo,⁴⁰ R. P. Guo,⁴⁷ Y. P. Guo,^{12,f} A. Guskov,^{35,a} X. T. H.,^{1,61} T. T. Han,⁴⁸ W. Y. Han,³⁸ X. Q. Hao,²⁰ F. A. Harris,⁶³ K. K. He,⁵³ K. L. He,^{1,61} F. H. H. Heinsius,⁴ C. H. Heinz,³⁴ Y. K. Heng,^{1,56,61} C. Herold,⁵⁸ T. Holtmann,⁴ P. C. Hong,^{12,f} G. Y. Hou,^{1,61} Y. R. Hou,⁶¹ Z. L. Hou,¹ H. M. Hu,^{1,61} J. F. Hu,^{54,i} T. Hu,^{1,56,61} Y. Hu,¹ G. S. Huang,^{69,56} K. X. Huang,⁵⁷ L. Q. Huang,^{30,61} X. T. Huang,⁴⁸ Y. P. Huang,¹ T. Hussain,⁷¹ N. Hüsken,^{27,34} W. Imoehl,²⁷ M. Irshad,^{69,56} J. Jackson,²⁷ S. Jaeger,⁴ S. Janchiv,³¹ J. H. Jeong,¹⁰ Q. Ji,¹ Q. P. Ji,²⁰ X. B. Ji,^{1,61} X. L. Ji,^{1,56} Y. Y. Ji,⁴⁸ Z. K. Jia,^{69,56} P. C. Jiang,^{45,g} S. S. Jiang,³⁸ T. J. Jiang,¹⁷ X. S. Jiang,^{1,56,61} Y. Jiang,⁶¹ J. B. Jiao,⁴⁸ Z. Jiao,²³ S. Jin,⁴¹ Y. Jin,⁶⁴ M. Q. Jing,^{1,61} T. Johansson,⁷³ X. K.,¹ S. Kabana,³² N. Kalantar-Nayestanaki,⁶² X. L. Kang,⁹ X. S. Kang,³⁹ R. Kappert,⁶² M. Kavatsyuk,⁶² B. C. Ke,⁷⁹ A. Khoukaz,⁶⁶ R. Kiuchi,¹ R. Kliemt,¹⁴ L. Koch,³⁶ O. B. Kolcu,^{60a} B. Kopf,⁴ M. K. Kuessner,⁴ A. Kupsc,^{43,73} W. Kühn,³⁶ J. J. Lane,⁶⁵ J. S. Lange,³⁶ P. Larin,¹⁹ A. Lavanaia,²⁶ L. Lavezzi,^{72a,72c} T. T. Lei,^{69,56} Z. H. Lei,^{69,56} H. Leithoff,³⁴ M. Lellmann,³⁴ T. Lenz,³⁴ C. Li,⁴⁶ C. Li,⁴² C. H. Li,³⁸ Cheng Li,^{69,56} D. M. Li,⁷⁹ F. Li,^{1,56} G. Li,¹ H. Li,^{69,56} H. B. Li,^{1,61} H. J. Li,²⁰ H. N. Li,^{54,i} Hui Li,⁴² J. R. Li,⁵⁹ J. S. Li,⁵⁷ J. W. Li,⁴⁸ Ke Li,¹ L. J. Li,^{1,61} L. K. Li,¹ Lei Li,³ M. H. Li,⁴² P. R. Li,^{37,j,k} S. X. Li,¹² T. Li,⁴⁸ W. D. Li,^{1,61} W. G. Li,¹ X. H. Li,^{69,56} X. L. Li,⁴⁸ Xiaoyu Li,^{1,61} Y. G. Li,^{45,g} Z. J. Li,⁵⁷ Z. X. Li,¹⁶ Z. Y. Li,⁵⁷ C. Liang,⁴¹ H. Liang,^{69,56} H. Liang,^{1,61} H. Liang,³³ Y. F. Liang,⁵² Y. T. Liang,^{30,61} G. R. Liao,¹⁵ L. Z. Liao,⁴⁸ J. Libby,²⁶ A. Limphirat,⁵⁸ D. X. Lin,^{30,61} T. Lin,¹ B. J. Liu,¹ B. X. Liu,⁷⁴ C. Liu,³³ C. X. Liu,¹ D. Liu,^{19,69} F. H. Liu,⁵¹ Fang Liu,¹ Feng Liu,⁶ G. M. Liu,^{54,i} H. Liu,^{37,j,k} H. B. Liu,¹⁶ H. M. Liu,^{1,61} Huanhuan Liu,¹ Huihui Liu,²¹ J. B. Liu,^{69,56} J. L. Liu,⁷⁰ J. Y. Liu,^{1,61} K. Liu,¹ K. Y. Liu,³⁹ Ke Liu,²² L. Liu,^{69,56} L. C. Liu,⁴² Lu Liu,⁴² M. H. Liu,^{12,f} P. L. Liu,¹ Q. Liu,⁶¹ S. B. Liu,^{69,56} T. Liu,^{12,f} W. K. Liu,⁴² W. M. Liu,^{69,56} X. Liu,^{37,j,k} Y. Liu,^{37,j,k} Y. B. Liu,⁴² Z. A. Liu,^{1,56,61} Z. Q. Liu,⁴⁸ X. C. Lou,^{1,56,61} F. X. Lu,⁵⁷ H. J. Lu,²³ J. G. Lu,^{1,56} X. L. Lu,¹ Y. Lu,⁷ Y. P. Lu,^{1,56} Z. H. Lu,^{1,61} C. L. Luo,⁴⁰ M. X. Luo,⁷⁸ T. Luo,^{12,f} X. L. Luo,^{1,56} X. R. Lyu,⁶¹ Y. F. Lyu,⁴² F. C. Ma,³⁹ H. L. Ma,¹ J. L. Ma,^{1,61} L. L. Ma,⁴⁸ M. M. Ma,^{1,61} Q. M. Ma,¹ R. Q. Ma,^{1,61} R. T. Ma,⁶¹ X. Y. Ma,^{1,56} Y. Ma,^{45,g} F. E. Maas,¹⁹ M. Maggiora,^{72a,72c} S. Maldaner,⁴ S. Malde,⁶⁷ A. Mangoni,^{28b} Y. J. Mao,^{45,g} Z. P. Mao,¹ S. Marcello,^{72a,72c} Z. X. Meng,⁶⁴ J. G. Messchendorp,^{14,62} G. Mezzadri,^{29a} H. Miao,^{1,61} T. J. Min,⁴¹ R. E. Mitchell,²⁷ X. H. Mo,^{1,56,61} N. Yu. Muchnoi,^{13,b} Y. Nefedov,³⁵ F. Nerling,^{19,d} I. B. Nikolaev,^{13,b} Z. Ning,^{1,56} S. Nisar,^{11,1} Y. Niu,⁴⁸ S. L. Olsen,⁶¹ Q. Ouyang,^{1,56,61} S. Pacetti,^{28b,28c} X. Pan,⁵³ Y. Pan,⁵⁵ A. Pathak,³³ P. Patteri,^{28a} Y. P. Pei,^{69,56} M. Pelizaeus,⁴ H. P. Peng,^{69,56} K. Peters,^{14,d} J. L. Ping,⁴⁰ R. G. Ping,^{1,61} S. Plura,³⁴ S. Pogodin,³⁵ V. Prasad,³² F. Z. Qi,¹ H. Qi,^{69,56} H. R. Qi,⁵⁹ M. Qi,⁴¹ T. Y. Qi,^{12,f} S. Qian,^{1,56} W. B. Qian,⁶¹ C. F. Qiao,⁶¹ J. J. Qin,⁷⁰ L. Q. Qin,¹⁵ X. P. Qin,^{12,f} X. S. Qin,⁴⁸ Z. H. Qin,^{1,56} J. F. Qiu,¹ S. Q. Qu,⁵⁹ C. F. Redmer,³⁴ K. J. Ren,³⁸ A. Rivetti,^{72c} V. Rodin,⁶² M. Rolo,^{72c} G. Rong,^{1,61} Ch. Rosner,¹⁹ S. N. Ruan,⁴² N. Salone,⁴³ A. Sarantsev,^{35,c} Y. Schelhaas,³⁴ K. Schoenning,⁷³ M. Scodreggio,^{29a,29b} K. Y. Shan,^{12,f} W. Shan,²⁴ X. Y. Shan,^{69,56} J. F. Shangguan,⁵³ L. G. Shao,^{1,61} M. Shao,^{69,56} C. P. Shen,^{12,f} H. F. Shen,^{1,61} W. H. Shen,⁶¹ X. Y. Shen,^{1,61} B. A. Shi,⁶¹ H. C. Shi,^{69,56} J. L. Shi,¹² J. Y. Shi,¹ Q. Q. Shi,⁵³ R. S. Shi,^{1,61} X. Shi,^{1,56} J. J. Song,²⁰ T. Z. Song,⁵⁷ W. M. Song,^{33,1} Y. J. Song,¹² Y. X. Song,^{45,g} S. Sosio,^{72a,72c} S. Spataro,^{72a,72c} F. Stieler,³⁴ Y. J. Su,⁶¹ G. B. Sun,⁷⁴ G. X. Sun,¹ H. Sun,⁶¹ H. K. Sun,¹ J. F. Sun,²⁰ K. Sun,⁵⁹ L. Sun,⁷⁴ S. S. Sun,^{1,61} T. Sun,^{1,61} W. Y. Sun,³³ Y. Sun,⁹ Y. J. Sun,^{69,56} Y. Z. Sun,¹ Z. T. Sun,⁴⁸ Y. X. Tan,^{69,56} C. J. Tang,⁵² G. Y. Tang,¹ J. Tang,⁵⁷ Y. A. Tang,⁷⁴ L. Y. Tao,⁷⁰ Q. T. Tao,^{25,h} M. Tat,⁶⁷ J. X. Teng,^{69,56} V. Thoren,⁷³ W. H. Tian,⁵⁷ W. H. Tian,⁵⁰ Z. F. Tian,⁷⁴ I. Uman,^{60b} B. Wang,¹ B. L. Wang,⁶¹ Bo Wang,^{69,56} C. W. Wang,⁴¹ D. Y. Wang,^{45,g} F. Wang,⁷⁰ H. J. Wang,^{37,j,k}


H. P. Wang,^{1,61} K. Wang,^{1,56} L. L. Wang,¹ M. Wang,⁴⁸ Meng Wang,^{1,61} S. Wang,^{37,j,k} S. Wang,^{12,f} T. Wang,^{12,f} T. J. Wang,⁴²
W. Wang,⁵⁷ W. Wang,⁷⁰ W. H. Wang,⁷⁴ W. P. Wang,^{69,56} X. Wang,^{45,g} X. F. Wang,^{37,j,k} X. J. Wang,³⁸ X. L. Wang,^{12,f}
Y. Wang,⁵⁹ Y. D. Wang,⁴⁴ Y. F. Wang,^{1,56,61} Y. H. Wang,⁴⁶ Y. N. Wang,⁴⁴ Y. Q. Wang,¹ Yaqian Wang,^{18,1} Yi Wang,⁵⁹
Z. Wang,^{1,56} Z. L. Wang,⁷⁰ Z. Y. Wang,^{1,61} Ziyi Wang,⁶¹ D. Wei,⁶⁸ D. H. Wei,¹⁵ F. Weidner,⁶⁶ S. P. Wen,¹
C. W. Wenzel,⁴ U. W. Wiedner,⁴ G. Wilkinson,⁶⁷ M. Wolke,⁷³ L. Wollenberg,⁴ C. Wu,³⁸ J. F. Wu,^{1,61} L. H. Wu,¹ L. J. Wu,^{1,61}
X. Wu,^{12,f} X. H. Wu,³³ Y. Wu,⁶⁹ Y. J. Wu,^{30,61} Z. Wu,^{1,56} L. Xia,^{69,56} X. M. Xian,³⁸ T. Xiang,^{45,g} D. Xiao,^{37,j,k} G. Y. Xiao,⁴¹
H. Xiao,^{12,f} S. Y. Xiao,¹ Y. L. Xiao,^{12,f} Z. J. Xiao,⁴⁰ C. Xie,⁴¹ X. H. Xie,^{45,g} Y. Xie,⁴⁸ Y. G. Xie,^{1,56} Y. H. Xie,⁶ Z. P. Xie,^{69,56}
T. Y. Xing,^{1,61} C. F. Xu,^{1,61} C. J. Xu,⁵⁷ G. F. Xu,¹ H. Y. Xu,⁶⁴ Q. J. Xu,¹⁷ W. Xu,^{1,61} W. L. Xu,⁶⁴ X. P. Xu,⁵³ Y. C. Xu,⁷⁶
Z. P. Xu,⁴¹ Z. S. Xu,⁶¹ F. Yan,^{12,f} L. Yan,^{12,f} W. B. Yan,^{69,56} W. C. Yan,⁷⁹ X. Q. Yan,¹ H. J. Yang,^{49,e}
H. L. Yang,³³ H. X. Yang,¹ Tao Yang,¹ Y. Yang,^{12,f} Y. F. Yang,⁴² Y. X. Yang,^{1,61} Yifan Yang,^{1,61} Z. W. Yang,^{37,j,k} M. Ye,^{1,56}
M. H. Ye,⁸ J. H. Yin,¹ Z. Y. You,⁵⁷ B. X. Yu,^{1,56,61} C. X. Yu,⁴² G. Yu,^{1,61} T. Yu,⁷⁰ X. D. Yu,^{45,g} C. Z. Yuan,^{1,61}
L. Yuan,² S. C. Yuan,¹ X. Q. Yuan,¹ Y. Yuan,^{1,61} Z. Y. Yuan,⁵⁷ C. X. Yue,³⁸ A. A. Zafar,⁷¹ F. R. Zeng,⁴⁸ X. Zeng,^{12,f}
Y. Zeng,^{25,h} Y. J. Zeng,^{1,61} X. Y. Zhai,³³ Y. H. Zhan,⁵⁷ A. Q. Zhang,^{1,61} B. L. Zhang,^{1,61} B. X. Zhang,¹ D. H. Zhang,⁴²
G. Y. Zhang,²⁰ H. Zhang,⁶⁹ H. H. Zhang,⁵⁷ H. H. Zhang,³³ H. Q. Zhang,^{1,56,61} H. Y. Zhang,^{1,56} J. J. Zhang,⁵⁰ J. Q. Zhang,⁴⁰
J. W. Zhang,^{1,56,61} J. X. Zhang,^{37,j,k} J. Y. Zhang,¹ J. Z. Zhang,^{1,61} Jianyu Zhang,⁶¹ Jiawei Zhang,^{1,61} L. M. Zhang,⁵⁹
L. Q. Zhang,⁵⁷ Lei Zhang,⁴¹ P. Zhang,¹ Q. Y. Zhang,^{38,79} Shuihan Zhang,^{1,61} Shulei Zhang,^{25,h} X. D. Zhang,⁴⁴
X. M. Zhang,¹ X. Y. Zhang,⁴⁸ X. Y. Zhang,⁵³ Y. Zhang,⁷⁰ Y. Zhang,⁶⁷ Y. T. Zhang,⁷⁹ Y. H. Zhang,^{1,56} Yan Zhang,^{69,56}
Yao Zhang,¹ Z. H. Zhang,¹ Z. L. Zhang,³³ Z. Y. Zhang,⁴² Z. Y. Zhang,⁷⁴ G. Zhao,¹ J. Zhao,³⁸ J. Y. Zhao,^{1,61}
J. Z. Zhao,^{1,56} Lei Zhao,^{69,56} Ling Zhao,¹ M. G. Zhao,⁴² S. J. Zhao,⁷⁹ Y. B. Zhao,^{1,56} Y. X. Zhao,^{30,61}
Z. G. Zhao,^{69,56} A. Zhemchugov,^{35,a} B. Zheng,⁷⁰ J. P. Zheng,^{1,56} W. J. Zheng,^{1,61} Y. H. Zheng,⁶¹ B. Zhong,⁴⁰ X. Zhong,⁵⁷
H. Zhou,⁴⁸ L. P. Zhou,^{1,61} X. Zhou,⁷⁴ X. K. Zhou,⁶ X. R. Zhou,^{69,56} X. Y. Zhou,³⁸ Y. Z. Zhou,^{12,f} J. Zhu,⁴²
K. Zhu,¹ K. J. Zhu,^{1,56,61} L. Zhu,³³ L. X. Zhu,⁶¹ S. H. Zhu,⁶⁸ S. Q. Zhu,⁴¹ T. J. Zhu,^{12,f} W. J. Zhu,^{12,f} Y. C. Zhu,^{69,56}
Z. A. Zhu,^{1,61} J. H. Zou,¹ and J. Zu^{69,56}

(BESIII Collaboration)

¹*Institute of High Energy Physics, Beijing 100049, People's Republic of China*²*Beihang University, Beijing 100191, People's Republic of China*³*Beijing Institute of Petrochemical Technology, Beijing 102617, People's Republic of China*⁴*Bochum Ruhr-University, D-44780 Bochum, Germany*⁵*Carnegie Mellon University, Pittsburgh, Pennsylvania 15213, USA*⁶*Central China Normal University, Wuhan 430079, People's Republic of China*⁷*Central South University, Changsha 410083, People's Republic of China*⁸*China Center of Advanced Science and Technology, Beijing 100190, People's Republic of China*⁹*China University of Geosciences, Wuhan 430074, People's Republic of China*¹⁰*Chung-Ang University, Seoul 06974, Republic of Korea*¹¹*COMSATS University Islamabad, Lahore Campus,**Defence Road, Off Raiwind Road, 54000 Lahore, Pakistan*¹²*Fudan University, Shanghai 200433, People's Republic of China*¹³*G.I. Budker Institute of Nuclear Physics SB RAS (BINP), Novosibirsk 630090, Russia*¹⁴*GSI Helmholtzcentre for Heavy Ion Research GmbH, D-64291 Darmstadt, Germany*¹⁵*Guangxi Normal University, Guilin 541004, People's Republic of China*¹⁶*Guangxi University, Nanning 530004, People's Republic of China*¹⁷*Hangzhou Normal University, Hangzhou 310036, People's Republic of China*¹⁸*Hebei University, Baoding 071002, People's Republic of China*¹⁹*Helmholtz Institute Mainz, Staudinger Weg 18, D-55099 Mainz, Germany*²⁰*Henan Normal University, Xinxiang 453007, People's Republic of China*²¹*Henan University of Science and Technology, Luoyang 471003, People's Republic of China*²²*Henan University of Technology, Zhengzhou 450001, People's Republic of China*²³*Huangshan College, Huangshan 245000, People's Republic of China*²⁴*Hunan Normal University, Changsha 410081, People's Republic of China*²⁵*Hunan University, Changsha 410082, People's Republic of China*²⁶*Indian Institute of Technology Madras, Chennai 600036, India*²⁷*Indiana University, Bloomington, Indiana 47405, USA*^{28a}*INFN Laboratori Nazionali di Frascati, I-00044, Frascati, Italy*

- ^{28b}*INFN Sezione di Perugia, I-06100, Perugia, Italy*
^{28c}*University of Perugia, I-06100, Perugia, Italy*
^{29a}*INFN Sezione di Ferrara, I-44122, Ferrara, Italy*
^{29b}*University of Ferrara, I-44122, Ferrara, Italy*
³⁰*Institute of Modern Physics, Lanzhou 730000, People's Republic of China*
³¹*Institute of Physics and Technology, Peace Avenue 54B, Ulaanbaatar 13330, Mongolia*
³²*Instituto de Alta Investigación, Universidad de Tarapacá, Casilla 7D, Arica, Chile*
³³*Jilin University, Changchun 130012, People's Republic of China*
³⁴*Johannes Gutenberg University of Mainz,
 Johann-Joachim-Becher-Weg 45, D-55099 Mainz, Germany*
³⁵*Joint Institute for Nuclear Research, 141980 Dubna, Moscow Region, Russia*
³⁶*Justus-Liebig-Universität Giessen, II. Physikalisches Institut,
 Heinrich-Buff-Ring 16, D-35392 Giessen, Germany*
³⁷*Lanzhou University, Lanzhou 730000, People's Republic of China*
³⁸*Liaoning Normal University, Dalian 116029, People's Republic of China*
³⁹*Liaoning University, Shenyang 110036, People's Republic of China*
⁴⁰*Nanjing Normal University, Nanjing 210023, People's Republic of China*
⁴¹*Nanjing University, Nanjing 210093, People's Republic of China*
⁴²*Nankai University, Tianjin 300071, People's Republic of China*
⁴³*National Centre for Nuclear Research, Warsaw 02-093, Poland*
⁴⁴*North China Electric Power University, Beijing 102206, People's Republic of China*
⁴⁵*Peking University, Beijing 100871, People's Republic of China*
⁴⁶*Qufu Normal University, Qufu 273165, People's Republic of China*
⁴⁷*Shandong Normal University, Jinan 250014, People's Republic of China*
⁴⁸*Shandong University, Jinan 250100, People's Republic of China*
⁴⁹*Shanghai Jiao Tong University, Shanghai 200240, People's Republic of China*
⁵⁰*Shanxi Normal University, Linfen 041004, People's Republic of China*
⁵¹*Shanxi University, Taiyuan 030006, People's Republic of China*
⁵²*Sichuan University, Chengdu 610064, People's Republic of China*
⁵³*Soochow University, Suzhou 215006, People's Republic of China*
⁵⁴*South China Normal University, Guangzhou 510006, People's Republic of China*
⁵⁵*Southeast University, Nanjing 211100, People's Republic of China*
⁵⁶*State Key Laboratory of Particle Detection and Electronics,
 Beijing 100049, Hefei 230026, People's Republic of China*
⁵⁷*Sun Yat-Sen University, Guangzhou 510275, People's Republic of China*
⁵⁸*Suranaree University of Technology, University Avenue 111,
 Nakhon Ratchasima 30000, Thailand*
⁵⁹*Tsinghua University, Beijing 100084, People's Republic of China*
^{60a}*Turkish Accelerator Center Particle Factory Group, Istinye University, 34010, Istanbul, Turkey*
^{60b}*Near East University, Nicosia, North Cyprus, 99138, Mersin 10, Turkey*
⁶¹*University of Chinese Academy of Sciences, Beijing 100049, People's Republic of China*
⁶²*University of Groningen, NL-9747 AA Groningen, The Netherlands*
⁶³*University of Hawaii, Honolulu, Hawaii 96822, USA*
⁶⁴*University of Jinan, Jinan 250022, People's Republic of China*
⁶⁵*University of Manchester, Oxford Road, Manchester M13 9PL, United Kingdom*
⁶⁶*University of Muenster, Wilhelm-Klemm-Strasse 9, 48149 Muenster, Germany*
⁶⁷*University of Oxford, Keble Road, Oxford OX13RH, United Kingdom*
⁶⁸*University of Science and Technology Liaoning, Anshan 114051, People's Republic of China*
⁶⁹*University of Science and Technology of China, Hefei 230026, People's Republic of China*
⁷⁰*University of South China, Hengyang 421001, People's Republic of China*
⁷¹*University of the Punjab, Lahore-54590, Pakistan*
^{72a}*University of Turin and INFN, University of Turin, I-10125, Turin, Italy*
^{72b}*University of Eastern Piedmont, I-15121, Alessandria, Italy*
^{72c}*INFN, I-10125, Turin, Italy*
⁷³*Uppsala University, Box 516, SE-75120 Uppsala, Sweden*
⁷⁴*Wuhan University, Wuhan 430072, People's Republic of China*
⁷⁵*Xinyang Normal University, Xinyang 464000, People's Republic of China*
⁷⁶*Yantai University, Yantai 264005, People's Republic of China*
⁷⁷*Yunnan University, Kunming 650500, People's Republic of China*

⁷⁸Zhejiang University, Hangzhou 310027, People's Republic of China
⁷⁹Zhengzhou University, Zhengzhou 450001, People's Republic of China

 (Received 15 March 2023; accepted 23 March 2023; published 18 April 2023; corrected 28 April 2023)

Using initial-state radiation events from a total integrated luminosity of 11.957 fb^{-1} of e^+e^- collision data collected at center-of-mass energies between 3.773 and 4.258 GeV with the BESIII detector at BEPCII, the cross section for the process $e^+e^- \rightarrow \Lambda\bar{\Lambda}$ is measured in 16 $\Lambda\bar{\Lambda}$ invariant mass intervals from the production threshold up to $3.00 \text{ GeV}/c^2$. The results are consistent with previous results from *BABAR* and BESIII, but with better precision and with narrower $\Lambda\bar{\Lambda}$ invariant mass intervals than *BABAR*.

DOI: 10.1103/PhysRevD.107.072005

I. INTRODUCTION

Electromagnetic form factors (EMFFs), which parametrize the inner structure of hadrons, are fundamental observables for understanding the strong interaction. In the timelike region, EMFFs are extensively studied in electron-positron collisions by measuring hadron pair production cross sections. For a spin-1/2 baryon (B), the cross section in the Born approximation of the one-photon-exchange process $e^+e^- \rightarrow B\bar{B}$ is parametrized in terms of electric and magnetic form factors G_E and G_M by [1]

$$\sigma^B(s) = \frac{4\pi\alpha^2 C\beta}{3s} \left[|G_M(s)|^2 + \frac{2m_B^2 c^2}{s} |G_E(s)|^2 \right], \quad (1)$$

where α is the fine-structure constant, C is the Coulomb correction factor [2], $\beta = \sqrt{1 - 4m_B^2 c^4/s}$ is a phase-space (PHSP) factor, s is the square of the c.m. energy, m_B is the mass of the baryon, and c is the speed of light. C accounts for the electromagnetic interaction of the fermions in the final state, and in the pointlike approximation, it is one for neutral baryons and $y/(1 - e^{-y})$ with $y = \pi\alpha\sqrt{1 - \beta^2}/\beta$ for charged baryons. Therefore, for charged baryon pairs, the factor of β due to PHSP is canceled by the Coulomb factor, which results in a nonzero cross section at the threshold when $\beta = 0$. However, there is no cancellation in the neutral baryon-pair case, so the cross section is zero.

There have been many experimental studies on the charged and neutral baryon-pair production cross sections in the past decades, such as $e^+e^- \rightarrow p\bar{p}$ [3,4], $e^+e^- \rightarrow n\bar{n}$ [5], $e^+e^- \rightarrow \Lambda\bar{\Lambda}$ [6–9], $e^+e^- \rightarrow \Sigma\bar{\Sigma}$ [10,11], $e^+e^- \rightarrow \Xi\bar{\Xi}$ [12,13], and $e^+e^- \rightarrow \Lambda_c^+\bar{\Lambda}_c^-$ [14]. Although the conclusions for some channels are questionable due to large uncertainties, there is a general tendency in the production cross sections for these baryon pairs to have a step near the threshold, which then decreases with the increase of the c.m. energy of the baryon pair [15].

The cross section of the process $e^+e^- \rightarrow \Lambda\bar{\Lambda}$ very close to the threshold has been measured in both the *BABAR* and the BESIII experiments. In the *BABAR* experiment, the cross section from the $\Lambda\bar{\Lambda}$ production threshold up to $M_{\Lambda\bar{\Lambda}} = 2.27 \text{ GeV}/c^2$ was measured as $204_{-60}^{+62} \pm 22 \text{ pb}$ [6]. This result indicates a possible nonzero cross section at threshold which is in conflict with Eq. (1). However, due to the wide $\Lambda\bar{\Lambda}$ mass interval and large uncertainties, a solid conclusion cannot be drawn. The BESIII experiment also measured the cross section at the c.m. energy (\sqrt{s}) of 2.2324 GeV, which is only 1.0 MeV above the $\Lambda\bar{\Lambda}$ production threshold, to be $305 \pm 45_{-36}^{+66} \text{ pb}$ [7]. This indicates a threshold enhancement phenomenon in the process $e^+e^- \rightarrow \Lambda\bar{\Lambda}$. Interestingly, in both the *BABAR*

^aAlso at the Moscow Institute of Physics and Technology, Moscow 141700, Russia.

^bAlso at Novosibirsk State University, Novosibirsk, 630090, Russia.

^cAlso at the NRC “Kurchatov Institute,” PNPI, 188300 Gatchina, Russia.

^dAlso at Goethe University Frankfurt, 60323 Frankfurt am Main, Germany.

^eAlso at Key Laboratory for Particle Physics, Astrophysics and Cosmology, Ministry of Education; Shanghai Key Laboratory for Particle Physics and Cosmology; Institute of Nuclear and Particle Physics, Shanghai 200240, People's Republic of China.

^fAlso at Key Laboratory of Nuclear Physics and Ion-beam Application (MOE) and Institute of Modern Physics, Fudan University, Shanghai 200443, People's Republic of China.

^gAlso at State Key Laboratory of Nuclear Physics and Technology, Peking University, Beijing 100871, People's Republic of China.

^hAlso at School of Physics and Electronics, Hunan University, Changsha 410082, China.

ⁱAlso at Guangdong Provincial Key Laboratory of Nuclear Science, Institute of Quantum Matter, South China Normal University, Guangzhou 510006, China.

^jAlso at Frontiers Science Center for Rare Isotopes, Lanzhou University, Lanzhou 730000, People's Republic of China.

^kAlso at Lanzhou Center for Theoretical Physics, Lanzhou University, Lanzhou 730000, People's Republic of China.

^lAlso at the Department of Mathematical Sciences, IBA, Karachi 75270, Pakistan.

Published by the American Physical Society under the terms of the Creative Commons Attribution 4.0 International license. Further distribution of this work must maintain attribution to the author(s) and the published article's title, journal citation, and DOI. Funded by SCOAP³.

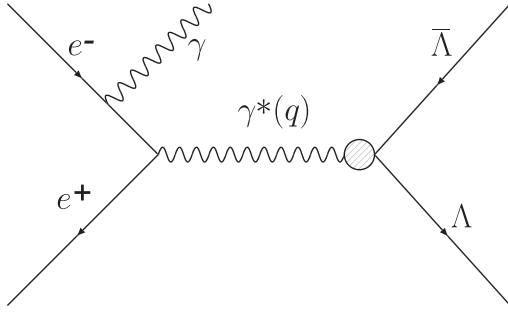


FIG. 1. The leading-order Feynman diagram for the ISR process $e^+e^- \rightarrow \gamma\Lambda\bar{\Lambda}$. The ISR photon can be emitted from the electron or the positron.

and BESIII experiments, a jump was observed in the process $e^+e^- \rightarrow K^+K^-K^+K^-$ near the $\Lambda\bar{\Lambda}$ production threshold [16,17].

To explain the near threshold enhancement, some theoretical studies have been performed, in which the effects of final-state radiation [18] and vector-meson resonances [19–21] have been taken into account. The enhancement in the case of neutral baryons may also be explained by an electromagnetic interaction occurring at the quark level [22]. However, experimentally, the cross section measurements of $e^+e^- \rightarrow \Lambda\bar{\Lambda}$ near threshold are still limited and more measurements are needed to further understand this phenomenon.

The cross section and EMFFs of the Λ hyperon have been measured via the annihilation channel $e^+e^- \rightarrow \Lambda\bar{\Lambda}$ using the energy scan technique [7–9], in which the c.m. energy of the collider is varied according to the experimental plan and the cross section is measured at each c.m. energy. In addition, the radiative return channel $e^+e^- \rightarrow \gamma\Lambda\bar{\Lambda}$ as illustrated in Fig. 1, where γ is a hard photon from the initial-state radiation (ISR) process, offers a technique complementary to the energy scan technique for the Λ hyperon cross section measurement. This technique has been used in the *BABAR* experiment to measure the cross section and effective form factor of the Λ hyperon [6].

The differential Born cross section for the $e^+e^- \rightarrow \gamma\Lambda\bar{\Lambda}$ process, integrated over the $\Lambda(\bar{\Lambda})$ momenta and the photon polar angle, is written as [23]

$$\frac{d\sigma_{e^+e^- \rightarrow \gamma\Lambda\bar{\Lambda}}(q^2)}{dq^2} = \frac{1}{s} W(s, x) \sigma_{\Lambda\bar{\Lambda}}(q^2), \quad (2)$$

where $\sigma_{\Lambda\bar{\Lambda}}(q^2)$ is the cross section for the $e^+e^- \rightarrow \Lambda\bar{\Lambda}$ process, q is the momentum transfer of the virtual photon whose squared value represents the invariant mass squared of $\Lambda\bar{\Lambda}$, $x = \frac{2E_\gamma^*}{\sqrt{s}} = 1 - \frac{q^2}{s}$, and E_γ^* is the energy of the ISR photon in the e^+e^- c.m. system. The function [24]

$$W(s, x) = kx^{k-1} \left[1 + \frac{\alpha}{\pi} \left(\frac{\pi^2}{3} - \frac{1}{2} \right) + \frac{3}{4}k \right. \\ \left. + k^2 \left(\frac{37}{96} - \frac{\pi^2}{12} - \frac{1}{72} \ln \frac{s}{m_e^2} \right) \right] - k \left(1 - \frac{1}{2}x \right) \\ + \frac{1}{8}k^2 \left[4(2-x) \ln \frac{1}{x} \right. \\ \left. - \frac{1 + 3(1-x)^2}{x} \ln(1-x) - 6 + x \right], \\ k = \frac{2\alpha}{\pi} \left[\ln \frac{s}{m_e^2} - 1 \right] \quad (3)$$

describes the probability for the emission of an ISR photon with energy fraction x , and m_e is the electron mass.

In this analysis, we present the measurement of the $e^+e^- \rightarrow \Lambda\bar{\Lambda}$ cross section from the production threshold up to 3.00 GeV/ c^2 using the ISR process $e^+e^- \rightarrow \gamma\Lambda\bar{\Lambda}$. The used datasets, corresponding to a total integrated luminosity of 11.957 fb $^{-1}$, are collected at 12 c.m. energies between 3.773 and 4.258 GeV with the BESIII detector [25] at the BEPCII Collider [26].

II. THE BESIII DETECTOR AND DATA SAMPLES

The BESIII detector [25] records symmetric e^+e^- collisions provided by the BEPCII storage ring [26] in the c.m. energy range from 2.00 up to 4.95 GeV, with a peak luminosity of 1×10^{33} cm $^{-2}$ s $^{-1}$ achieved at $\sqrt{s} = 3.77$ GeV. BESIII has collected large data samples in this energy region [27]. The cylindrical core of the BESIII detector covers 93% of the full solid angle and consists of a helium-based multilayer drift chamber (MDC), a plastic scintillator time-of-flight system (TOF), and a CsI(Tl) electromagnetic calorimeter (EMC), which are all enclosed in a superconducting solenoidal magnet providing a 1.0 T magnetic field [28]. The solenoid is supported by an octagonal flux-return yoke with resistive plate counter muon identification modules interleaved with steel. The charged particle momentum resolution at 1 GeV/ c is 0.5%, and the dE/dx resolution is 6% for electrons from Bhabha scattering. The EMC measures photon energies with a resolution of 2.5% (5%) at 1 GeV in the barrel (end cap) region. The time resolution in the TOF barrel region is 68 ps, while that in the end cap region used to be 110 ps. The end cap TOF system was updated in 2015 using multigap resistive plate chamber technology, providing a time resolution of 60 ps [29–31].

The experimental datasets used in this analysis are listed in Table I. To optimize the event selection criteria, Monte Carlo (MC) simulations are performed with GEANT4-based [32] software, which includes the description of geometry and material, the detector response and the digitization model, as well as a database for the detector running conditions and performances. In this analysis, the

TABLE I. The c.m. energy \sqrt{s} [42,43] and the integrated luminosity \mathcal{L}_{int} [44–46] of the datasets used in the present analysis.

\sqrt{s} (GeV)	\mathcal{L}_{int} (pb $^{-1}$)
3.773	2931.8
4.128	401.5
4.157	408.7
4.178	3189.0
4.189	526.7
4.199	526.0
4.209	517.1
4.219	514.6
4.226	1047.3
4.236	530.3
4.244	538.1
4.258	825.7

event generator ConExc [33] is used to generate the signal process $e^+e^- \rightarrow \gamma\Lambda\bar{\Lambda}$ ($\Lambda \rightarrow p\pi^-$, $\bar{\Lambda} \rightarrow \bar{p}\pi^+$) with one million events at the different c.m. energies up to ISR leading order (LO), i.e., with only one ISR photon, and vacuum polarization (VP) is included. The selection efficiencies are estimated by the signal MC samples. An alternative event generator, PHOKHARA10.0 [34], is used to study the systematic uncertainty of the MC model. The cross section line shape used for the generation of the signal MC samples is from Ref. [35]. Inclusive MC samples at $\sqrt{s} = 3.773$ and 4.178 GeV are used to investigate possible background contamination. They consist of inclusive hadronic processes ($e^+e^- \rightarrow q\bar{q}$, $q = u, d, s$) modeled with the LUARLW [36] at $\sqrt{s} = 3.773$ GeV and KKMC [37,38] at $\sqrt{s} = 4.178$ GeV, and the ISR production of vector charmonium states [$e^+e^- \rightarrow \gamma J/\psi$, $\gamma\psi(2S)$, $\gamma\psi(3773)$] generated with BesEvtGen [39] using the VECTORISR model [40,41]. In addition, several exclusive MC samples are generated to study the background, with different event generators and models.

III. EVENT SELECTION

The complete process we study is $e^+e^- \rightarrow \gamma\Lambda\bar{\Lambda} \rightarrow \gamma(p\pi^-)(\bar{p}\pi^+)$, with the final state $\gamma p\pi^-\bar{p}\pi^+$, where γ is the ISR photon. To provide a clean sample in the threshold region, the ISR photon is detected (tagged). However, the differential cross section of the ISR reaction (such as $e^+e^- \rightarrow \gamma\Lambda\bar{\Lambda}$) as a function of the ISR photon polar angle reaches its highest value when the photon is emitted at a small angle relative to the direction of the electron (or positron) beam [23]. Since this is out of the angular acceptance of the EMC, photons falling in this region cannot be detected, resulting in a reduction of signal efficiency. Moreover, the detection efficiency is further reduced by the low momenta of the pions, which, according

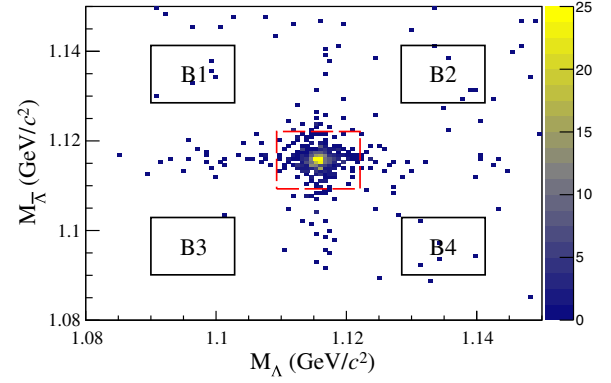


FIG. 2. Distribution of $M_{\bar{\Lambda}}$ versus M_{Λ} of the accepted candidates in mode I from all datasets. The dashed red box encloses the signal region, while the black boxes show the sideband regions.

to the study of the signal MC samples, are mostly less than 0.2 GeV/c. We categorize the reconstruction of signal candidates into two modes: mode I corresponds to fully reconstructed events, i.e., all particles in the final state are identified; in mode II, a partial reconstruction method with a missing pion is used to increase the efficiency.

Charged tracks detected in the MDC are required to be within $|\cos\theta| < 0.93$, where θ is the polar angle with respect to the z axis, which is the symmetry axis of the MDC. The distance of closest approach of each charged track to the interaction point must be less than 30 cm along the z direction and less than 10 cm in the transverse plane. For each signal candidate, at least three charged tracks are required.

The combined information of dE/dx and TOF is used to calculate particle identification (PID) probabilities for the pion, kaon, and proton hypotheses, and the particle type with the highest probability is assigned to the track.

A secondary vertex fit is performed to obtain the decay vertex of the $\Lambda(\bar{\Lambda})$ candidate, and the $\Lambda(\bar{\Lambda})$ candidate is reconstructed by fitting the $p\pi^-(\bar{p}\pi^+)$ tracks to a common decay vertex. If there is more than one $\Lambda(\bar{\Lambda})$ candidate, the one with the minimum chi-square value of the secondary vertex fit is selected. The reconstructed mass of the $\Lambda(\bar{\Lambda})$ candidate, $M_{\Lambda}(M_{\bar{\Lambda}})$, is required to be within 6.4 MeV/ c^2 of the nominal Λ mass, m_{Λ} , from the Particle Data Group (PDG) [47], as shown in Fig. 2. There is no requirement on the decay length of $\Lambda(\bar{\Lambda})$. Both a Λ and a $\bar{\Lambda}$ are required in mode I, while either a Λ or a $\bar{\Lambda}$ is required in mode II.

Information on the electromagnetic showers in the EMC is used to select the photon candidates. It is required that the shower time is within 700 ns of the event's start time to suppress electronic noise and energy deposits unrelated to the events. A photon candidate is selected if its deposited energy is greater than 0.4 GeV. For each candidate signal event, at least one photon is required which is considered as the ISR photon.

A kinematic fit is applied to further suppress background. For mode I, a four-constraint (4C) kinematic

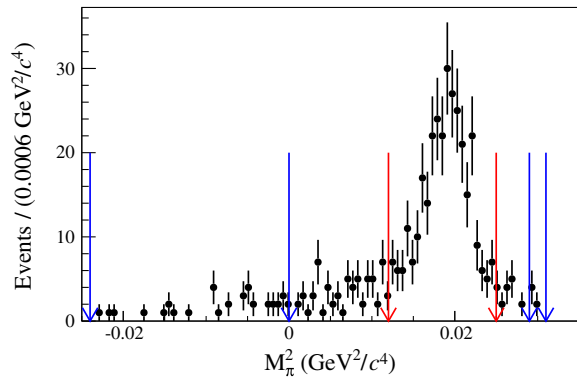


FIG. 3. The M_π^2 spectrum of the accepted candidates in mode II from all datasets. The region between the red arrows is the signal region, and the regions between the blue arrows are the sideband regions.

fit requiring energy-momentum conservation under the hypothesis of a $\gamma\Lambda\bar{\Lambda}$ final state is applied to the signal candidates. If there is more than one photon candidate, the combination with the minimum χ_{4C}^2 is selected. To suppress the background with one more photon than the signal process, we require $\chi_{4C}^2 \leq \chi_{4C,\gamma\gamma}^2$, where χ_{4C}^2 and $\chi_{4C,\gamma\gamma}^2$ are the chi-square values under the hypotheses of $\gamma\Lambda\bar{\Lambda}$ and $\gamma\gamma\Lambda\bar{\Lambda}$ final states. For mode II, a one-constraint (1C) kinematic fit with a missing $\pi^+(\pi^-)$ under the hypothesis of a $\gamma\Lambda\bar{p}\pi^+(\gamma\bar{\Lambda}p\pi^-)$ final state is applied to the signal candidates. Combining all $\gamma\bar{p}(\gamma p)$ pairs with the reconstructed $\Lambda(\bar{\Lambda})$, 1C kinematic fits are applied with the invariant mass of $\bar{p}\pi^+(p\pi^-)$ being constrained to the nominal Λ mass [47] and the mass of $\pi^+(\pi^-)$ being unconstrained. The $\gamma\bar{p}(\gamma p)$ combination with the minimum χ_{1C}^2 is selected, where χ_{1C}^2 is the chi-square of the 1C kinematic fit. A requirement of $\chi_{4C}^2 \leq 50$

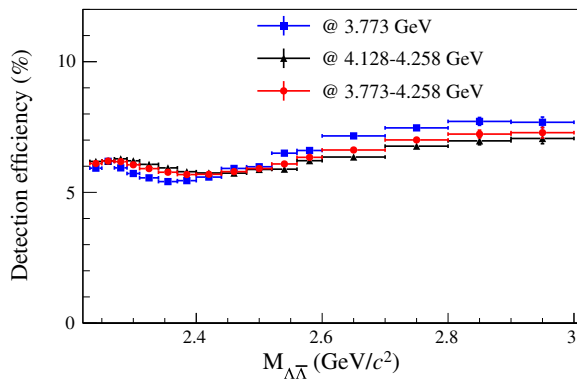


FIG. 4. The $M_{\Lambda\bar{\Lambda}}$ -dependent selection efficiencies obtained from MC simulation. Squares (blue), triangles (black), and circles (red) with error bars represent the datasets at $\sqrt{s} = 3.773, 4.178\text{--}4.258,$ and $3.773\text{--}4.258$ GeV, respectively. The combined efficiency is weighted according to the effective luminosity of the ISR process.

($\chi_{1C}^2 \leq 5$) is optimized for the signal candidates for mode I (mode II).

For the candidates of mode II, the distribution of the mass squared of the missing π (M_π^2), obtained from energy-momentum conservation, is shown in Fig. 3. To suppress background, a requirement of $0.012 \leq M_\pi^2 \leq 0.025$ GeV^2/c^4 is applied.

The distribution of the selection efficiencies obtained from signal MC samples as a function of invariant mass of $\Lambda\bar{\Lambda}$ ($M_{\Lambda\bar{\Lambda}}$) is shown in Fig. 4, where the efficiencies at the c.m. energies between 4.128 and 4.258 GeV are combined and weighted according to the effective luminosity of the ISR process. It should be noted that, to improve the mass resolution of $M_{\Lambda\bar{\Lambda}}$, we correct $M_{\Lambda\bar{\Lambda}}$ to $(M_{\Lambda\bar{\Lambda}} - M_\Lambda - M_{\bar{\Lambda}} + 2 \times m_\Lambda)$. The mass resolution is given by the root-mean-square deviation of $(M_{\Lambda\bar{\Lambda}} - M_{\Lambda\bar{\Lambda}}^{\text{truth}})$ of the signal MC sample, where $M_{\Lambda\bar{\Lambda}}^{\text{truth}}$ is the set value of the invariant mass of $\Lambda\bar{\Lambda}$ when generating the MC events. In this paper, the correction of the $M_{\Lambda\bar{\Lambda}}$ is implied unless specified. The $M_{\Lambda\bar{\Lambda}}$ spectrum of the accepted candidates from all datasets is shown in Fig. 5, in which 817 events are retained. The contributions from $J/\psi \rightarrow \Lambda\bar{\Lambda}$ and $\psi(2S) \rightarrow \Lambda\bar{\Lambda}$ decays are clearly seen. About 60% of the signal candidates have $M_{\Lambda\bar{\Lambda}}$ below 3.00 GeV/c^2 , and the number of signal candidates (N_{obs}) in each $M_{\Lambda\bar{\Lambda}}$ interval is listed in the first column of Table II.

IV. BACKGROUND ANALYSIS

Potential background channels are investigated in the inclusive MC samples with a topology analysis [48]; they consist of channels containing $\Lambda\bar{\Lambda}$ and channels without $\Lambda\bar{\Lambda}$. The background channels containing $\Lambda\bar{\Lambda}$, such as the processes of $e^+e^- \rightarrow \pi^0\Lambda\bar{\Lambda}$, $e^+e^- \rightarrow \gamma(\Lambda\bar{\Sigma}^0 + \text{c.c.})$, and $e^+e^- \rightarrow \gamma J/\psi(\psi(2S))$ with $J/\psi(\psi(2S))$ decaying to $\gamma\Lambda\bar{\Lambda}$, are studied individually, while the non- $\Lambda\bar{\Lambda}$ background is estimated with the sideband method.

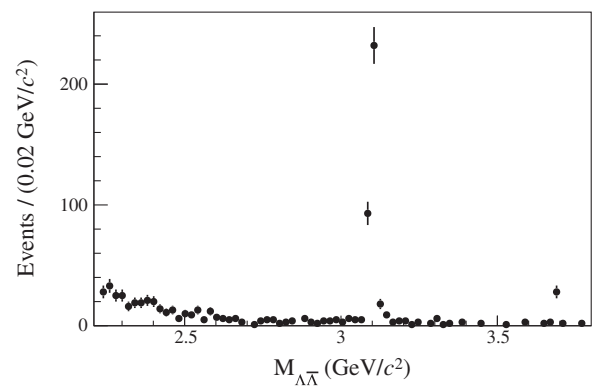


FIG. 5. The $M_{\Lambda\bar{\Lambda}}$ spectrum for events satisfying the $\gamma\Lambda\bar{\Lambda}$ selection criteria from all datasets. Contributions from $J/\psi \rightarrow \Lambda\bar{\Lambda}$ and $\psi(2S) \rightarrow \Lambda\bar{\Lambda}$ decays are clearly seen.

TABLE II. The number of signal candidates (N_{obs}), number of $\pi^0\Lambda\bar{\Lambda}$ events ($N_{\pi^0}^{\text{bkg}}$), number of $\gamma(\Lambda\bar{\Sigma}^0 + \text{c.c.})$ events ($N_{\Lambda\Sigma}^{\text{bkg}}$), and number of non- $\Lambda\bar{\Lambda}$ events ($N_{\text{non-}\Lambda\bar{\Lambda}}^{\text{bkg}}$), in each $M_{\Lambda\bar{\Lambda}}$ interval, for the whole dataset. The uncertainties are statistical.

$M_{\Lambda\bar{\Lambda}}(\text{GeV}/c^2)$	N_{obs}	$N_{\pi^0}^{\text{bkg}}$	$N_{\Lambda\Sigma}^{\text{bkg}}$	$N_{\text{non-}\Lambda\bar{\Lambda}}^{\text{bkg}}$
2.231–2.250	28.0 ± 5.3	1.9 ± 1.2	1.28 ± 0.05	0.63 ± 0.70
2.25–2.27	32.0 ± 5.7	$0.7^{+0.6}_{-0.5}$	1.35 ± 0.05	$-0.41^{+1.61}_{-0.02}$
2.27–2.29	25.0 ± 5.0	1.4 ± 0.6	1.36 ± 0.05	2.67 ± 1.22
2.29–2.31	24.0 ± 4.9	1.3 ± 0.6	1.37 ± 0.05	0.69 ± 0.71
2.31–2.34	28.0 ± 5.3	2.4 ± 0.7	2.00 ± 0.07	$0.08^{+1.24}_{-0.50}$
2.34–2.37	27.0 ± 5.2	4.2 ± 0.9	1.83 ± 0.05	$0.11^{+1.24}_{-0.50}$
2.37–2.40	34.0 ± 5.8	5.2 ± 0.9	1.54 ± 0.05	$-0.32^{+1.61}_{-0.02}$
2.40–2.44	28.0 ± 5.3	3.5 ± 0.8	1.74 ± 0.05	$0.10^{+1.24}_{-0.50}$
2.44–2.48	23.0 ± 4.8	3.3 ± 0.7	1.53 ± 0.05	$-0.32^{+1.61}_{-0.02}$
2.48–2.52	16.0 ± 4.0	3.3 ± 0.7	1.28 ± 0.05	$1.22^{+1.43}_{-0.87}$
2.52–2.56	19.0 ± 4.4	1.7 ± 0.5	1.01 ± 0.05	1.51 ± 0.90
2.56–2.60	18.0 ± 4.2	1.4 ± 0.5	0.87 ± 0.05	$-0.21^{+1.61}_{-0.02}$
2.60–2.70	24.0 ± 4.9	1.4 ± 0.5	1.74 ± 0.05	$-0.39^{+1.61}_{-0.02}$
2.70–2.80	15.0 ± 3.9	1.5 ± 0.5	1.12 ± 0.04	3.00 ± 1.25
2.80–2.90	15.0 ± 3.9	2.3 ± 0.6	0.73 ± 0.03	$0.07^{+1.17}_{-0.25}$
2.90–3.00	18.0 ± 4.2	2.6 ± 0.7	0.49 ± 0.03	$0.36^{+1.24}_{-0.50}$

Events of $e^+e^- \rightarrow \pi^0\Lambda\bar{\Lambda}$ are easily mistaken as signal events if a soft photon from the high-energy π^0 is missing. A data-driven method is used to estimate their contribution. A sample of $\pi^0\Lambda\bar{\Lambda}$ events is selected from data, and its background is estimated with the sideband method. The sideband regions are chosen in the distribution of the invariant mass of $\gamma\gamma$ ($M_{\gamma\gamma}$). The number of events of this sample is calculated by $N_{\pi^0}^{\text{data}} = N_{\pi^0}^{\text{SigReg}} - N_{\pi^0}^{\text{Side}}/2$, where $N_{\pi^0}^{\text{SigReg}}$ and $N_{\pi^0}^{\text{Side}}$ are the numbers of events from the signal and the sideband regions of the $\pi^0\Lambda\bar{\Lambda}$ sample, respectively. Next, the contribution from the remaining $\pi^0\Lambda\bar{\Lambda}$ background ($N_{\pi^0}^{\text{bkg}}$) in the signal candidates is determined by

$$N_{\pi^0}^{\text{bkg}} = N_{\pi^0}^{\text{data}} \times \frac{N_{\text{ISR}}^{\text{MC}}}{N_{\pi^0}^{\text{MC}}}, \quad (4)$$

where $N_{\text{ISR}}^{\text{MC}}$ and $N_{\pi^0}^{\text{MC}}$ are the numbers of the events selected by the signal and $\pi^0\Lambda\bar{\Lambda}$ selection criteria from the $\pi^0\Lambda\bar{\Lambda}$ MC sample. The $\pi^0\Lambda\bar{\Lambda}$ MC sample is generated with the ConExc [33] event generator up to ISR LO, and the line shape is obtained with the datasets collected at c.m. energies from 2.644 to 3.080 GeV by BESIII.

In the reaction $e^+e^- \rightarrow \gamma(\Lambda\bar{\Sigma}^0 + \text{c.c.})$, the $\Sigma^0(\bar{\Sigma}^0)$ decays to $\gamma\Lambda(\bar{\Lambda})$ with a branching ratio of 100% [47], where the γ has low energy. Therefore, if the photon from the $\Sigma^0(\bar{\Sigma}^0)$ decay is missing, this event can be misidentified as signal. To estimate the background from this reaction, a MC sample with a total of two million events is generated

with the ConExc [33] event generator up to ISR LO, and the line shape used to generate the MC events is determined with the datasets collected at c.m. energies from 2.309 to 3.080 GeV by BESIII. After applying the signal ($\gamma\Lambda\bar{\Lambda}$) selection criteria to this sample, we obtain the number of the surviving $\gamma(\Lambda\bar{\Sigma}^0 + \text{c.c.})$ events ($N_{\Lambda\Sigma}^{\text{MC}}$). A scaling factor is obtained by $f = N_{\text{exp}}/N_{\text{gen}}$, where N_{exp} is the expected number of the $\gamma(\Lambda\bar{\Sigma}^0 + \text{c.c.})$ events estimated with the ($\Lambda\bar{\Sigma}^0 + \text{c.c.})$ cross section line shape, and N_{gen} is the number of MC simulated events. Finally, the number of $\gamma(\Lambda\bar{\Sigma}^0 + \text{c.c.})$ background events ($N_{\Lambda\Sigma}^{\text{bkg}}$) is estimated by $N_{\Lambda\Sigma}^{\text{bkg}} = f \times N_{\Lambda\Sigma}^{\text{MC}}$. Some other background channels, such as the processes $e^+e^- \rightarrow \eta\Lambda\bar{\Lambda}$ and $e^+e^- \rightarrow \gamma J/\psi(\psi(2S))$, are negligible.

Next, the sideband method is used to study the non- $\Lambda\bar{\Lambda}$ background. For mode I, two-dimensional (2D) sideband regions of M_{Λ} versus $M_{\bar{\Lambda}}$ are adopted, and for mode II, one-dimensional (1D) sideband regions in the distribution of M_{π}^2 are used. The distributions of $M_{\Lambda(\bar{\Lambda})}$ and M_{π}^2 of inclusive MC samples after removing the channels containing the $\Lambda\bar{\Lambda}$ pair are nearly flat, so it is reasonable to use the sideband method. The 2D sideband regions (shown in Fig. 2) are chosen as follows: B1, $1.0901 \leq M_{\Lambda} \leq 1.1029$ and $1.1285 \leq M_{\bar{\Lambda}} \leq 1.1413$ GeV/ c^2 ; B2, $1.1285 \leq M_{\Lambda} \leq 1.1413$ and $1.1285 \leq M_{\bar{\Lambda}} \leq 1.1413$ GeV/ c^2 ; B3, $1.0901 \leq M_{\Lambda} \leq 1.1029$ and $1.0901 \leq M_{\bar{\Lambda}} \leq 1.1029$ GeV/ c^2 ; and B4, $1.1285 \leq M_{\Lambda} \leq 1.1413$ and $1.0901 \leq M_{\bar{\Lambda}} \leq 1.1029$ GeV/ c^2 . The 1D sideband regions (shown in Fig. 3) are chosen as $-0.024 \leq M_{\pi}^2 \leq 0$ and $0.029 \leq M_{\pi}^2 \leq 0.031$ GeV $^2/c^4$. The numbers of events from sideband regions of data ($N_{\text{non-}\Lambda\bar{\Lambda}}^{\text{data}}$) are calculated by

$$N_{\text{non-}\Lambda\bar{\Lambda}}^{\text{data}} = \frac{1}{4} \times N_{2\text{D}} + \frac{1}{2} \times N_{1\text{D}}, \quad (5)$$

where $N_{2\text{D}}$ and $N_{1\text{D}}$ are the numbers of the events from the 2D and 1D sideband regions of data, respectively. The same sideband regions are used for the $\pi^0\Lambda\bar{\Lambda}$ and $\gamma(\Lambda\bar{\Sigma}^0 + \text{c.c.})$ MC samples, and the numbers of events from sideband regions of these MC samples ($N_{\text{non-}\Lambda\bar{\Lambda}}^{\text{MC}}$) are obtained with Eq. (5). The number of non- $\Lambda\bar{\Lambda}$ background events ($N_{\text{non-}\Lambda\bar{\Lambda}}^{\text{bkg}}$) is estimated by

$$N_{\text{non-}\Lambda\bar{\Lambda}}^{\text{bkg}} = N_{\text{non-}\Lambda\bar{\Lambda}}^{\text{data}} - N_{\text{non-}\Lambda\bar{\Lambda}}^{\text{MC}}. \quad (6)$$

The numbers of events for the three main background channels above ($N_{\pi^0}^{\text{bkg}}$, $N_{\Lambda\Sigma}^{\text{bkg}}$, $N_{\text{non-}\Lambda\bar{\Lambda}}^{\text{bkg}}$) are calculated in each $M_{\Lambda\bar{\Lambda}}$ interval when measuring the Born cross section.

The distributions of $M_{\Lambda\bar{\Lambda}}$ of the main background events from all datasets are shown in Fig. 6, and the numbers of background events over all datasets for the three main background channels in each $M_{\Lambda\bar{\Lambda}}$ interval are listed in Table II.

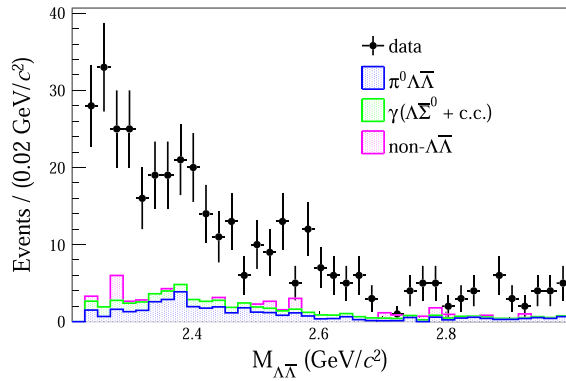


FIG. 6. The distributions of $M_{\Lambda\bar{\Lambda}}$ for the signal candidates and the main background events from all datasets. Black dots with error bars refer to the signal candidates, and blue, green, and magenta histograms represent the $\pi^0\Lambda\bar{\Lambda}$, $\gamma(\Lambda\Sigma^0 + c.c.)$, and non- $\Lambda\bar{\Lambda}$ background events, respectively.

V. SYSTEMATIC UNCERTAINTY

Several sources of systematic uncertainties are considered in the cross section measurement. The combined results of different reconstructed methods and different datasets are summarized in Tables III and IV for the correlated and uncorrelated parts, respectively. The correlated and uncorrelated parts are summed in quadrature to determine the total uncertainty.

The integrated luminosity is measured with an uncertainty of 0.5% at $\sqrt{s} = 3.773$ GeV and an uncertainty of 1.0% at other c.m. energies [44–46]. In this analysis, the effective luminosity of the ISR process is calculated based on Eq. (3), and a 0.5% uncertainty is estimated [49]. Thus, the total systematic uncertainty on the luminosity is 0.8% at $\sqrt{s} = 3.773$ GeV and 1.2% at other energy points.

The uncertainties from the reconstruction of Λ and $\bar{\Lambda}$ are studied by a control sample of $J/\psi \rightarrow pK^-\bar{\Lambda} + c.c.$ and determined to be 2.8% and 3.8% at $\sqrt{s} = 3.773$ GeV, and 2.6% and 3.4% at other energy points, respectively. A 1.0% uncertainty is taken for the ISR photon detection [50].

TABLE III. The correlated systematic uncertainties (in %) on the cross section measurement. $\mathcal{B}(\Lambda \rightarrow p\pi)$ is the branching ratio of $\Lambda(\bar{\Lambda}) \rightarrow p\pi^-(\bar{p}\pi^+)$.

Source	Uncertainty
Luminosity	1.1
Λ reconstruction	2.1
$\bar{\Lambda}$ reconstruction	2.8
$\mathcal{B}(\Lambda \rightarrow p\pi)$	1.6
$p(\bar{p})$ tracking and PID	0.7
M_π^2 window	0.6
ISR photon detection	1.0
Kinematic fit	1.7
Neglected background	1.5
Total	4.7

TABLE IV. The uncorrelated systematic uncertainties (in %) in each $M_{\Lambda\bar{\Lambda}}$ interval on the cross section measurement: the uncertainty associated with the $\pi^0\Lambda\bar{\Lambda}$ channel ($\pi^0\Lambda\bar{\Lambda}$), $\gamma(\Lambda\Sigma^0 + c.c.)$ channel ($\gamma\Lambda\Sigma^0$), non- $\Lambda\bar{\Lambda}$ background (non- $\Lambda\bar{\Lambda}$), Λ angular distribution (Ang), and signal MC model (MC). The last column is the total uncorrelated systematic uncertainty.

$M_{\Lambda\bar{\Lambda}}$ (GeV/ c^2)	$\pi^0\Lambda\bar{\Lambda}$	$\gamma\Lambda\Sigma^0$	non- $\Lambda\bar{\Lambda}$	Ang	MC	Total
2.231–2.250	0.3	0.6	0.4	2.7	1.6	3.2
2.25–2.27	0.1	0.9	1.4	0.6	1.4	2.2
2.27–2.29	0.7	1.8	0.5	2.3	4.1	5.1
2.29–2.31	0.9	1.9	0.4	2.2	0.7	3.1
2.31–2.34	1.3	3.6	0.5	2.7	1.5	4.9
2.34–2.37	0.8	3.0	0.4	1.6	0.9	3.6
2.37–2.40	1.0	2.0	3.3	0.3	0.9	4.1
2.40–2.44	0.6	3.0	0.4	0.8	0.8	3.2
2.44–2.48	0.5	2.4	0.5	1.7	2.2	3.6
2.48–2.52	1.6	5.2	5.2	2.2	2.2	8.2
2.52–2.56	1.0	5.4	0.9	1.7	3.3	6.7
2.56–2.60	0.5	2.9	0.4	0.8	1.8	3.6
2.60–2.70	0.9	3.2	0.9	2.5	1.4	4.4
2.70–2.80	7.1	9.3	24.8	2.1	1.9	27.5
2.80–2.90	1.7	2.3	2.3	2.1	1.5	4.4
2.90–3.00	1.2	1.5	0.3	1.9	5.4	6.0

For mode II, the uncertainties due to the $p(\bar{p})$ tracking and PID are 1.0% for each [51]. The uncertainty due to the M_π^2 ($M_{\pi^\pm}^2$) window is also studied by the control sample of $J/\psi \rightarrow pK^-\bar{\Lambda} + c.c.$ and estimated as 1.4% (0.8%) at $\sqrt{s} = 3.773$ GeV and 1.5% (0.9%) at other energy points. The uncertainty due to the branching fraction of $\Lambda(\bar{\Lambda}) \rightarrow p\pi^-(\bar{p}\pi^+)$, $\mathcal{B}(\Lambda \rightarrow p\pi)$, is obtained from the PDG [47] to be 1.6%.

The uncertainty from the kinematic fit is divided into two parts: the contribution of the ISR photon and the contribution of the remainder. The former is determined by a control sample of the radiative Bhabha process $e^+e^- \rightarrow \gamma e^+e^-$ and estimated as 0.4%, 0.2%, and 1.1% for the cases of full reconstruction, missing π^- , and missing π^+ , respectively. The latter is studied by a control sample of $J/\psi \rightarrow \Lambda\bar{\Lambda}$ and is 0.2% (0.2%), 2.4% (2.2%), and 2.2% (2.2%) at $\sqrt{s} = 3.773$ GeV (other energy points), for the cases of full reconstruction, missing π^- , and missing π^+ , respectively. Thus, the uncertainty due to the kinematic fit at $\sqrt{s} = 3.773$ GeV (other energy points) is 0.6% (0.6%), 2.6% (2.4%), and 3.3% (3.3%) for the cases of full reconstruction, missing π^- , and missing π^+ , respectively.

The signal MC samples are generated with PHSP. The angular distribution of the $\Lambda\bar{\Lambda}$ pair, the spin correlation between Λ and $\bar{\Lambda}$, and the polarization of $\Lambda(\bar{\Lambda})$ decay are not taken into account. To estimate the uncertainty due to these factors, signal MC samples with an angular amplitude including these effects are generated. The parametrization of the angular amplitude is the same as that in Ref. [8], and the corresponding parameters are cited from it when

$M_{\Lambda\bar{\Lambda}} \leq 2.52 \text{ GeV}/c^2$ and obtained with the dataset at $\sqrt{s} = 2.900 \text{ GeV}$ when $M_{\Lambda\bar{\Lambda}} \geq 2.52 \text{ GeV}/c^2$. The relative difference of the detection efficiency to that of the PHSP mode is regarded as the uncertainty.

The uncertainty from the MC model is considered by changing the event generator from ConExc [33] to PHOKHARA10.0 [34]. The relative difference of the detection efficiency of these two event generators is taken as the uncertainty.

For the channel of $e^+e^- \rightarrow \pi^0\Lambda\bar{\Lambda}$, the sideband regions on the $M_{\gamma\gamma}$ spectrum are used to estimate the background of the $\pi^0\Lambda\bar{\Lambda}$ sample. Here, the 2D sideband regions (sideband of M_{Λ} and $M_{\bar{\Lambda}}$) and 3D sideband regions (sideband of M_{Λ} , $M_{\bar{\Lambda}}$, and $M_{\gamma\gamma}$) are also used. The values of $|\frac{N_{M_{\gamma\gamma}} - N_{2D}}{N_{\text{sig}}}|$ and $|\frac{N_{M_{\gamma\gamma}} - N_{3D}}{N_{\text{sig}}}|$ are obtained, where N_{sig} is the number of signal events, and $N_{M_{\gamma\gamma}}$, N_{2D} , and N_{3D} are the estimated numbers of $\pi^0\Lambda\bar{\Lambda}$ events based on $M_{\gamma\gamma}$, 2D, and 3D sidebands, respectively. The larger of the two values is taken as the uncertainty of this channel.

For the channel of $e^+e^- \rightarrow \gamma(\Lambda\bar{\Sigma}^0 + \text{c.c.})$, one of the parameters of the line shape is changed by adding and subtracting a standard deviation ($\pm 1\sigma$). Based on the different line shapes, different estimated numbers of $\gamma(\Lambda\bar{\Sigma}^0 + \text{c.c.})$ events are obtained. Further, the same method as for the $e^+e^- \rightarrow \pi^0\Lambda\bar{\Lambda}$ channel is used here to obtain the uncertainty of this channel.

For the non- $\Lambda\bar{\Lambda}$ background, we move the sideband regions by $0.002 \text{ GeV}/c^2$ and $0.002 \text{ GeV}^2/c^4$ toward the signal for the 2D and the 1D sidebands, respectively, and obtain the new estimated numbers of non- $\Lambda\bar{\Lambda}$ background events. The relative difference between the old and new results is regarded as the uncertainty. For the $M_{\Lambda\bar{\Lambda}}$ interval of $2.70\text{--}2.80 \text{ GeV}/c^2$, since N_{sig} is extremely small (0.8 ± 2.3) at $\sqrt{s} = 3.773 \text{ GeV}$, the estimation of this uncertainty at $\sqrt{s} = 3.773 \text{ GeV}$ is significantly larger than that in other intervals. Except for the three main background sources mentioned above, several other background channels are neglected, and their contribution is considered as a systematic uncertainty, which is 2.2% at $\sqrt{s} = 3.773 \text{ GeV}$ and 1.1% at other energy points.

In this analysis, 12 datasets are used and 3 reconstruction methods (full reconstruction and partial reconstruction with missing π^- or π^+) are applied. We divide the datasets into two groups, where the first group only includes the dataset at $\sqrt{s} = 3.773 \text{ GeV}$ and the second group includes the other datasets at c.m. energies from 4.128 to 4.258 GeV. The uncertainties of the second group are studied together or inherited from the result at $\sqrt{s} = 4.178 \text{ GeV}$. Thus, the systematic uncertainties are combined in two steps, where the first step combines the three reconstruction methods in each group and the second step combines the two groups. Uncertainties of the three reconstruction methods (two dataset groups) are combined as the average value weighted

by detection efficiencies (products of detection efficiency and effective luminosity). The weighted average formula is

$$\sigma_{\text{tot}}^2 = \sum_{i=1}^{3(2)} \omega_i^2 \sigma_i^2 + \sum_{i,j=1;i \neq j}^{3(2)} \rho_{ij} \omega_i \omega_j \sigma_i \sigma_j, \quad (7)$$

with

$$\omega_i = \frac{\varepsilon_i}{\sum_{i=1}^3 \varepsilon_i} \left(\omega_i = \frac{\varepsilon_i \mathcal{L}_i}{\sum_{i=1}^2 \varepsilon_i \mathcal{L}_i} \right), \quad (8)$$

where ω_i , σ_i , and ε_i with $i = 1, 2, 3$ ($i = 1, 2$) are the weight, systematic uncertainty, and efficiency for the reconstruction method (dataset group) i , and ρ_{ij} is the correlation parameter for two different reconstruction methods (dataset groups) i and j , and \mathcal{L}_i is the effective luminosity for the dataset group i . For the systematic uncertainties arising from background, the ρ_{ij} values are set to 0, and for other systematic uncertainties the ρ_{ij} are set to 1.

VI. RESULTS OF THE CROSS SECTION

The cross section for $e^+e^- \rightarrow \Lambda\bar{\Lambda}$ is calculated from the $M_{\Lambda\bar{\Lambda}}$ spectrum by

$$\sigma_{\Lambda\bar{\Lambda}}(M_{\Lambda\bar{\Lambda}}) = \frac{(dN_{\text{sig}}/dM_{\Lambda\bar{\Lambda}})}{\varepsilon \cdot \mathcal{B}(\Lambda \rightarrow p\pi) \cdot d\mathcal{L}_{\text{int}}/dM_{\Lambda\bar{\Lambda}}}, \quad (9)$$

where $(dN_{\text{sig}}/dM_{\Lambda\bar{\Lambda}})$ is the $M_{\Lambda\bar{\Lambda}}$ spectrum of data corrected for resolution effects after subtracting the background, ε is the detection efficiency from MC simulation as a function of $M_{\Lambda\bar{\Lambda}}$, and $\mathcal{B}(\Lambda \rightarrow p\pi) = 0.639 \pm 0.005$ [47]. The effective ISR luminosity $d\mathcal{L}_{\text{int}}/dM_{\Lambda\bar{\Lambda}}$ is calculated by $d\mathcal{L}_{\text{int}}/dM_{\Lambda\bar{\Lambda}} = W(s, x) \cdot \mathcal{L}_{\text{int}}$, where $W(s, x)$ is described by Eq. (3). This effective luminosity includes the first-order radiative correction but does not take into account VP, so the obtained cross section is the ‘‘dressed’’ cross section.

The dependence of the mass resolution on $M_{\Lambda\bar{\Lambda}}$ is determined, and accordingly the $M_{\Lambda\bar{\Lambda}}$ is divided into 16 intervals from the threshold up to $3.00 \text{ GeV}/c^2$. To reduce the impact of the mass resolution, the width of the $M_{\Lambda\bar{\Lambda}}$ bin is at least 5 times larger than the mass resolution, so we do not correct the mass spectrum for resolution effects. The measured cross sections for the process $e^+e^- \rightarrow \Lambda\bar{\Lambda}$ in these intervals are listed in Table V. A comparison between the results of this work and those of previous ones [6–9] is displayed in Fig. 7.

A search for a threshold effect is made by performing a least chi-square fit to the cross section from the production threshold up to 3.00 GeV with different assumed functions. The systematic uncertainty is included in the fit with the correlated and uncorrelated parts considered separately.

The first fit function is a perturbative QCD (pQCD)-driven energy power function [52]

TABLE V. The cross section (σ) of the whole dataset. N_{sig} is the total number of signal events, $\bar{\epsilon}$ is the average detection efficiency of 12 energy points weighted by the effective ISR luminosity, and \mathcal{L} is the total effective ISR luminosity. The uncertainties for N_{sig} are statistical. For σ , the first uncertainties are statistical, and the second are systematic.

$M_{\Lambda\bar{\Lambda}}$ (GeV/ c^2)	N_{sig}	$\bar{\epsilon}$	\mathcal{L} (pb $^{-1}$)	σ (pb)
2.231–2.250	24.1 ± 5.5	0.061	3.95	$245 \pm 56 \pm 14$
2.25–2.27	$30.3^{+5.7}_{-5.9}$	0.062	4.24	$283^{+53}_{-55} \pm 15$
2.27–2.29	19.5 ± 5.2	0.062	4.32	$179 \pm 48 \pm 13$
2.29–2.31	20.7 ± 5.0	0.061	4.41	$190 \pm 46 \pm 11$
2.31–2.34	$23.5^{+5.4}_{-5.5}$	0.059	6.78	$144^{+32.7}_{-33.5} \pm 9.8$
2.34–2.37	$20.8^{+5.3}_{-6.1}$	0.058	6.99	$126.6^{+32.1}_{-32.9} \pm 7.5$
2.37–2.40	$27.6^{+5.9}_{-6.1}$	0.057	7.20	$165^{+35}_{-37} \pm 11$
2.40–2.44	$22.7^{+5.4}_{-5.5}$	0.057	9.95	$98.1^{+23.2}_{-23.7} \pm 5.6$
2.44–2.48	$18.5^{+4.9}_{-5.1}$	0.058	10.37	$75.2^{+19.7}_{-20.8} \pm 4.5$
2.48–2.52	$10.2^{+4.2}_{-4.3}$	0.059	10.82	$38.9^{+15.9}_{-16.5} \pm 3.7$
2.52–2.56	14.7 ± 4.5	0.061	11.30	$52.4 \pm 16.0 \pm 4.3$
2.56–2.60	$15.9^{+4.3}_{-4.6}$	0.063	11.80	$52.1^{+14.0}_{-14.9} \pm 3.1$
2.60–2.70	$21.2^{+4.9}_{-5.2}$	0.066	31.96	$24.6^{+5.7}_{-6.0} \pm 1.6$
2.70–2.80	9.4 ± 4.1	0.070	35.96	$9.1 \pm 4.0 \pm 2.6$
2.80–2.90	$11.9^{+3.9}_{-4.1}$	0.072	40.76	$9.9^{+3.3}_{-3.4} \pm 0.7$
2.90–3.00	$14.5^{+4.3}_{-4.5}$	0.073	46.59	$10.5^{+3.1}_{-3.2} \pm 0.8$

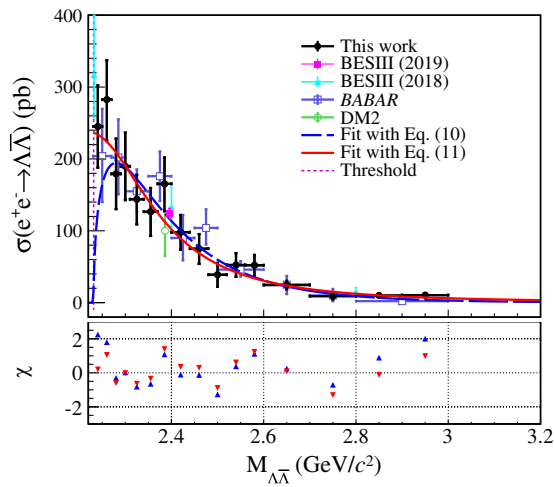


FIG. 7. The cross section for the $e^+e^- \rightarrow \Lambda\bar{\Lambda}$ process from this analysis (black dots with error bars) with comparison to previous works (see the legend in the figure) [6–9]. Both statistical and systematic uncertainties are included. The blue dashed line is the fit result using Eq. (10), and the red solid line is the fit result using Eq. (11). The vertical dashed line is the production threshold for $e^+e^- \rightarrow \Lambda\bar{\Lambda}$. The χ distributions of the two fits are shown in the bottom panel, where the blue and red triangles represent the results of Eqs. (10) and (11), respectively.

$$\sigma(s) = \frac{c_0 \cdot \beta(s) \cdot C}{(\sqrt{s} - c_1)^{10}}, \quad (10)$$

where c_0 and c_1 are free parameters and the Coulomb correction factor is $C = 1$ for neutral baryons. The fit result is shown as the blue dashed line in Fig. 7, with $c_0 = (1.07 \pm 0.74) \times 10^3 \text{ pb} \cdot \text{GeV}^{10}$, $c_1 = 1.27 \pm 0.08 \text{ GeV}$, and the fit quality $\chi^2/\text{d.o.f.} = 19.06/14$.

In Fig. 7, the pQCD prediction does not describe the anomalous enhancement well near threshold. Therefore, inspired by the results of cross section measurements of $e^+e^- \rightarrow n\bar{n}$ and $e^+e^- \rightarrow p\bar{p}$ [3,5], it is assumed that there is a step near the threshold for the $e^+e^- \rightarrow \Lambda\bar{\Lambda}$ cross section, the threshold enhancement effect. By taking into account the strong interaction near the threshold instead of using the formula of Eq. (10), which contains the Coulomb factor, the cross section can be expressed as [3]

$$\sigma(s) = \frac{e^{a_0} \pi^2 \alpha_s^3}{s \left[1 - e^{-\frac{\pi \alpha_s}{\beta}} \right] \left[1 + \left(\frac{\sqrt{s} - 2m_\Lambda}{a_1} \right)^{a_2} \right]}, \quad (11)$$

where a_0 , a_1 , and a_2 are three free parameters. The symbol α_s represents the strong running coupling constant and is parametrized as

$$\alpha_s = \left[\frac{1}{\alpha_s(m_Z^2)} + \frac{7}{4\pi} \ln \left(\frac{s}{m_Z^2} \right) \right]^{-1}, \quad (12)$$

where $m_Z = 91.1876 \text{ GeV}/c^2$ [47] is the mass of Z boson and $\alpha_s(m_Z^2) = 0.11856$. This fit has $\chi^2/\text{d.o.f.} = 9.83/13$, with $a_0 = 19.5 \pm 0.16$, $a_1 = 0.17 \pm 0.04 \text{ GeV}$, and $a_2 = 1.98 \pm 0.34$, and the fit result is shown as the red solid line in Fig. 7.

VII. STUDY OF THE $J/\psi \rightarrow \Lambda\bar{\Lambda}$ DECAY

The branching fraction of $J/\psi \rightarrow \Lambda\bar{\Lambda}$, $\mathcal{B}(J/\psi \rightarrow \Lambda\bar{\Lambda})$, is determined via the ISR process $e^+e^- \rightarrow \gamma J/\psi \rightarrow \gamma \Lambda\bar{\Lambda}$ at $\sqrt{s} = 3.773$ and 4.178 GeV . After integrating over the photon polar angle, the cross section for ISR production of a narrow resonance (vector meson V), such as J/ψ , decaying into the final state f is given by [53]

$$\sigma(s) = \frac{12\pi^2 \Gamma(V \rightarrow e^+e^-) \mathcal{B}(V \rightarrow f)}{m_V s} W(s, x_0), \quad (13)$$

where m_V and $\Gamma(V \rightarrow e^+e^-)$ are the mass and electronic width of the vector meson V , $x_0 = 1 - m_V^2/s$, $\mathcal{B}(V \rightarrow f)$ is the branching fraction of $V \rightarrow f$, and $W(s, x_0)$ is calculated by Eq. (3). If the cross section is measured, the branching fraction can be calculated by Eq. (13). The cross section can also be written as

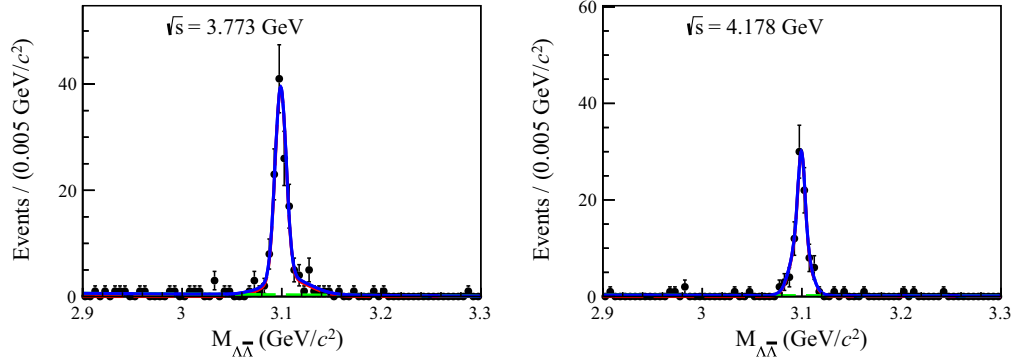


FIG. 8. Simultaneous fit (blue curve) with a double Gaussian function (red dashed curve) for the resonance and a linear function (green dashed curve) for background of the $M_{\Lambda\bar{\Lambda}}$ spectra at $\sqrt{s} = 3.773$ and 4.178 GeV. Black dots with error bars represent data.

$$\sigma(s) = \frac{N_{J/\psi}}{\varepsilon \cdot \mathcal{B}^2(\Lambda \rightarrow p\pi) \cdot \mathcal{L}_{\text{int}}}, \quad (14)$$

where $N_{J/\psi}$ is the number of J/ψ events, ε is the detection efficiency, and \mathcal{L}_{int} is the integrated luminosity of data, whose values are listed in Table I. The detection efficiency is estimated from MC simulation as 7.2% at $\sqrt{s} = 3.773$ GeV and 7.1% at $\sqrt{s} = 4.178$ GeV. The angular distribution of Λ in $J/\psi \rightarrow \Lambda\bar{\Lambda}$ decay is described by $1 + \alpha \cos^2 \theta_\Lambda$ with $\alpha = 0.469$ [54]. To determine $N_{J/\psi}$, using $\mathcal{B}(J/\psi \rightarrow \Lambda\bar{\Lambda})$ as a shared parameter, a simultaneous fit is performed with a double Gaussian function for the resonance and a linear function for the background and the continuum contribution, and the result is shown in Fig. 8.

For the systematic uncertainties on the measurement of $\mathcal{B}(J/\psi \rightarrow \Lambda\bar{\Lambda})$, the uncertainties of the luminosity, Λ and $\bar{\Lambda}$ reconstruction, $p(\bar{p})$ tracking and PID, M_π^2 window, ISR photon detection, $\mathcal{B}(\Lambda \rightarrow p\pi)$, and kinematic fit are the same as the cross section measurement. The uncertainty due to the MC model is assigned as 1.3%, by changing the model for the generation of the $J/\psi \rightarrow \Lambda\bar{\Lambda}$ decay. The uncertainty of the fit region is determined by changing the fit region from (2.90, 3.30) GeV/c^2 to a wider (2.80, 3.30) GeV/c^2 and a narrower interval (3.00, 3.20) GeV/c^2 to be 1.3%. The uncertainty from the signal model of the fit is estimated by changing the model from the double Gaussian function to the MC-shape-convolved Gaussian function as 1.3%. The uncertainty of the background model of the fit is estimated by changing the model from a linear function to a constant as 0.5%. Finally, we consider a systematic uncertainty due to the non- $\Lambda\bar{\Lambda}$ background. The non- $\Lambda\bar{\Lambda}$ background is treated as a peaking background, instead of a nonpeaking one as default. The relative difference between the results of the two strategies, 1.9%, is regarded as the uncertainty. The total uncertainty is obtained to be 5.6% by summing all uncertainties in quadrature.

$\mathcal{B}(J/\psi \rightarrow \Lambda\bar{\Lambda})$ is determined to be $(1.64 \pm 0.12 \pm 0.09) \times 10^{-3}$, where the first uncertainty is statistical and the second is systematic. It is consistent with the PDG value $(1.89 \pm 0.09) \times 10^{-3}$ [47] within 2σ .

VIII. SUMMARY AND DISCUSSION

Based on datasets corresponding to a total integrated luminosity of 11.957 fb^{-1} collected at 12 c.m. energies between 3.773 and 4.258 GeV with the BESIII detector at BEPCII, the cross section for the process $e^+e^- \rightarrow \Lambda\bar{\Lambda}$ is measured as the function of $M_{\Lambda\bar{\Lambda}}$ in 16 intervals from the production threshold up to $3.00 \text{ GeV}/c^2$ using ISR events with the ISR photon tagged. A partial reconstruction method allowing a charged π to be missing is used in addition to the full reconstruction method to increase the efficiency. In the first $M_{\Lambda\bar{\Lambda}}$ interval ranging from the threshold up to $2.25 \text{ GeV}/c^2$ (with the width of $19 \text{ MeV}/c^2$), the cross section is determined to be $245 \pm 56 \pm 13 \text{ pb}$, where the first uncertainty is statistical and the second is systematic. It is a nonzero value with a statistical significance of 4.3σ and larger than the pQCD prediction by 2.3σ . In the region from 2.25 up to $3.00 \text{ GeV}/c^2$, the cross section is measured in 15 intervals. The results are consistent with previous measurements at BABAR and BESIII. The spectrum of the cross section is fitted with the pQCD assumption and with the assumption of a step existing near threshold, with the latter being a better description of the data.

ACKNOWLEDGMENTS

The BESIII Collaboration thanks the staff of BEPCII, the IHEP computing center, and the supercomputing center of USTC for their strong support. This work is supported in part by National Key R&D Program of China under Contracts No. 2020YFA0406400 and No. 2020YFA0406300; National Natural Science Foundation of China (NSFC) under Contracts No. 11635010, No. 11735014, No. 11835012, No. 11935015,

No. 11935016, No. 11935018, No. 11961141012, No. 12022510, No. 12025502, No. 12035009, No. 12035013, No. 12192260, No. 12192261, No. 12192262, No. 12192263, No. 12192264, No. 12192265, No. 12275320, No. 11625523, No. 11705192, No. 11950410506, No. 12061131003, No. 12105276, and No. 12122509; the Chinese Academy of Sciences (CAS) Large-Scale Scientific Facility Program; the CAS Center for Excellence in Particle Physics (CCEPP); Joint Large-Scale Scientific Facility Funds of the NSFC and CAS under Contracts No. U1832207, No. U1732263, No. U1832103, and No. U2032111; CAS Key Research Program of Frontier Sciences under Contracts No. QYZDJ-SSW-SLH003 and No. QYZDJ-SSW-SLH040; 100 Talents Program of CAS; The Institute of Nuclear and Particle Physics (INPAC) and Shanghai Key Laboratory for Particle Physics and Cosmology; ERC under Contract No. 758462; European Union's Horizon 2020 Research

and Innovation Programme under Marie Skłodowska-Curie Grant Agreement under Contract No. 894790; German Research Foundation DFG under Contracts No. 443159800 and No. 455635585, Collaborative Research Center CRC 1044, FOR5327, GRK 2149; Istituto Nazionale di Fisica Nucleare, Italy; Ministry of Development of Turkey under Contract No. DPT2006K-120470; National Research Foundation of Korea under Contract No. NRF-2022R1A2C1092335; National Science and Technology fund; National Science Research and Innovation Fund (NSRF) via the Program Management Unit for Human Resources & Institutional Development, Research and Innovation under Contract No. B16F640076; Polish National Science Centre under Contract No. 2019/35/O/ST2/02907; the Royal Society, UK under Contracts No. DH140054 and No. DH160214; the Swedish Research Council; U.S. Department of Energy under Award No. DE-FG02-05ER41374.

-
- [1] N. Cabibbo and R. Gatto, *Phys. Rev.* **124**, 1577 (1961).
 [2] S. J. Brodsky and R. F. Lebed, *Phys. Rev. Lett.* **102**, 213401 (2009).
 [3] M. Ablikim *et al.* (BESIII Collaboration), *Phys. Rev. Lett.* **124**, 042001 (2020).
 [4] J. P. Lees *et al.* (BABAR Collaboration), *Phys. Rev. D* **87**, 092005 (2013).
 [5] M. Ablikim *et al.* (BESIII Collaboration), *Nat. Phys.* **17**, 1200 (2021).
 [6] B. Aubert *et al.* (BABAR Collaboration), *Phys. Rev. D* **76**, 092006 (2007).
 [7] M. Ablikim *et al.* (BESIII Collaboration), *Phys. Rev. D* **97**, 032013 (2018).
 [8] M. Ablikim *et al.* (BESIII Collaboration), *Phys. Rev. Lett.* **123**, 122003 (2019).
 [9] D. Bisello *et al.* (DM2 Collaboration), *Z. Phys. C* **48**, 23 (1990).
 [10] M. Ablikim *et al.* (BESIII Collaboration), *Phys. Lett. B* **814**, 136110 (2021).
 [11] M. Ablikim *et al.* (BESIII Collaboration), *Phys. Lett. B* **831**, 137187 (2022).
 [12] M. Ablikim *et al.* (BESIII Collaboration), *Phys. Rev. D* **103**, 012005 (2021).
 [13] M. Ablikim *et al.* (BESIII Collaboration), *Phys. Lett. B* **820**, 136557 (2021).
 [14] M. Ablikim *et al.* (BESIII Collaboration), *Phys. Rev. Lett.* **120**, 132001 (2018).
 [15] G. Huang and R. B. Ferroli (BESIII Collaboration), *Nat. Sci. Rev.* **8**, nwab187 (2021).
 [16] J. P. Lees *et al.* (BABAR Collaboration), *Phys. Rev. D* **86**, 012008 (2012).
 [17] M. Ablikim *et al.* (BESIII Collaboration), *Phys. Rev. D* **100**, 032009 (2019).
 [18] J. Haidenbauer and U. G. Meißner, *Phys. Lett. B* **761**, 456 (2016).
 [19] X. Cao, J. P. Dai, and Y. P. Xie, *Phys. Rev. D* **98**, 094006 (2018).
 [20] Y. Yang, D. Y. Chen, and Z. Lu, *Phys. Rev. D* **100**, 073007 (2019).
 [21] J. Sonnenschein and D. Weissman, *Nucl. Phys.* **B920**, 319 (2017).
 [22] R. Baldini, S. Pacetti, A. Zallo, and A. Zichichi, *Eur. Phys. J. A* **39**, 315 (2009).
 [23] V. P. Druzhinin, S. I. Eidelman, S. I. Serednyakov, and E. P. Solodov, *Rev. Mod. Phys.* **83**, 1545 (2011).
 [24] E. A. Kuraev and V. S. Fadin, *Sov. J. Nucl. Phys.* **41**, 466 (1985).
 [25] M. Ablikim *et al.* (BESIII Collaboration), *Nucl. Instrum. Methods Phys. Res., Sect. A* **614**, 345 (2010).
 [26] Y. F. Wang, *Int. J. Mod. Phys. A* **21**, 5371 (2006).
 [27] M. Ablikim *et al.* (BESIII Collaboration), *Chin. Phys. C* **44**, 040001 (2020).
 [28] K. X. Huang *et al.*, *Nucl. Sci. Tech.* **33**, 142 (2022).
 [29] X. Li *et al.*, *Radiat. Detect. Technol. Methods* **1**, 13 (2017).
 [30] Y. X. Guo *et al.*, *Radiat. Detect. Technol. Methods* **1**, 15 (2017).
 [31] P. Cao *et al.*, *Nucl. Instrum. Methods Phys. Res., Sect. A* **953**, 163053 (2020).
 [32] S. Agostinelli *et al.* (GEANT4 Collaboration), *Nucl. Instrum. Methods Phys. Res., Sect. A* **506**, 250 (2003).
 [33] R. G. Ping, *Chin. Phys. C* **38**, 083001 (2014).
 [34] Monte Carlo event generator PHOKHARA, <https://looptreeduality.csic.es/phokhara/>.
 [35] Z. Y. Li, A. X. Dai, and J. J. Xie, *Chin. Phys. Lett.* **39**, 011201 (2022).
 [36] M. Ablikim *et al.* (BESIII Collaboration), *Phys. Rev. Lett.* **128**, 062004 (2022).

- [37] S. Jadach, B. F. L. Ward, and Z. Was, *Phys. Rev. D* **63**, 113009 (2001).
- [38] S. Jadach, B. F. L. Ward, and Z. Was, *Comput. Phys. Commun.* **130**, 260 (2000).
- [39] R. G. Ping, *Chin. Phys. C* **32**, 599 (2008).
- [40] G. Bonneau and F. Martin, *Nucl. Phys.* **B27**, 381 (1971).
- [41] D. J. Lange, *Nucl. Instrum. Methods Phys. Res., Sect. A* **462**, 152 (2001).
- [42] M. Ablikim *et al.* (BESIII Collaboration), *Chin. Phys. C* **40**, 063001 (2016).
- [43] M. Ablikim *et al.* (BESIII Collaboration), *Chin. Phys. C* **45**, 103001 (2021).
- [44] M. Ablikim *et al.* (BESIII Collaboration), *Phys. Lett. B* **753**, 629 (2016); **812**, 135982(E) (2021).
- [45] M. Ablikim *et al.* (BESIII Collaboration), *Chin. Phys. C* **39**, 093001 (2015).
- [46] M. Ablikim *et al.* (BESIII Collaboration), *Chin. Phys. C* **46**, 113002 (2022).
- [47] R. L. Workman *et al.* (Particle Data Group), *Prog. Theor. Exp. Phys.* **2022**, 083C01 (2022).
- [48] X. Zhou, S. Du, G. Li, and C. Shen, *Comput. Phys. Commun.* **258**, 107540 (2021).
- [49] C. Noh, *New Phys. Sae Mulli* **71**, 1096 (2021).
- [50] M. Ablikim *et al.* (BESIII Collaboration), *Phys. Rev. D* **99**, 011101 (2019).
- [51] M. Ablikim *et al.* (BESIII Collaboration), *Phys. Rev. D* **91**, 112004 (2015).
- [52] S. Pacetti, R. Baldini Ferroli, and E. Tomasi-Gustafsson, *Phys. Rep.* **550**, 1 (2015).
- [53] M. Benayoun, S. I. Eidelman, V. N. Ivanchenko, and Z. K. Silagadze, *Mod. Phys. Lett. A* **14**, 2605 (1999).
- [54] M. Ablikim *et al.* (BESIII Collaboration), *Phys. Rev. D* **95**, 052003 (2017).

Correction: A second affiliation indicator was inserted and a byline footnote indicator was removed for author T. T. Lei.